

Seismological observations on the 2019 March 21 accidental explosion at Xiangshui chemical plant in Jiangsu, China

Yishan Song,^{1,2} Lian-Feng Zhao^{1,3}, Xiao-Bi Xie,⁴ Xiao Ma,^{1,2} Guilin Du,^{5,6} Xiaofeng Tian⁷ and Zhen-Xing Yao¹

¹Key Laboratory of Earth and Planetary Physics, Institute of Geology and Geophysics, Chinese Academy of Sciences, Beijing 100029, China.

E-mail: zhaolf@mail.iggcas.ac.cn

²College of Earth and Planetary Sciences, University of Chinese Academy of Sciences, Beijing, 100049, China

³Mohe Observatory of Geophysics, Institute of Geology and Geophysics, Chinese Academy of Sciences, Beijing 100029, China

⁴Institute of Geophysics and Planetary Physics, University of California at Santa Cruz, Santa Cruz, CA 95064, USA

⁵College of Earth Science and Engineering, Shandong University of Science and Technology, Qingdao 266590, China

⁶Weihai Earthquake Monitoring Center, Weihai 264200, China

⁷Geophysical Exploration Center, China Earthquake Administration, Zhengzhou 450002, China

Accepted 2021 August 27. Received 2021 August 16; in original form 2021 March 22

SUMMARY

On 2019 March 21, an explosion accidentally occurred at a chemical plant in Xiangshui, Yancheng City, Jiangsu Province, China. Using broad-band digital seismic data from East China, South Korea and Japan, we investigate properties of the Xiangshui explosion as well as two nearby chemical explosions and four nearby natural earthquakes in Jiangsu Province, East China. From Lg and Rayleigh waves recorded by regional networks, both body wave magnitude m_b (Lg) and surface wave magnitude M_s (Rayleigh) are calculated for these events. The magnitudes of the Xiangshui explosion are m_b (Lg) = 3.39 ± 0.24 and M_s = 1.95 ± 0.27 , respectively. Both the empirical magnitude–yield relation for buried explosion and empirical yield–crater dimension relation for open-pit explosion are adopted for investigating the explosive yield. The result from the yield–crater dimension relation is approximately 492 ton, which is consistent with the ground truth and considerably larger than that from the buried source model. This also reveals that, for Xiangshui explosion, the explosion to seismic energy conversion rate is approximately one-third compared to a similar sized fully confined explosion. By comparing the body wave and surface wave magnitudes from explosions and nearby earthquakes, we find that the $m_b:M_s$ discriminant calculated at regional distances cannot properly distinguish explosions from natural earthquakes. However, the P/S spectral ratios Pg/Lg, Pn/Lg and Pn/Sn from the same data set can be good discriminants for identifying explosions from earthquakes.

Key words: Body waves; Earthquake monitoring and test-ban treaty verification; Earthquake source observations; Seismic attenuation; Wave propagation.

1 INTRODUCTION

An explosion at a chemical plant hit Xiangshui, Yancheng City in Jiangsu Province, East China on 2019 March 21 (Fig. 1). According to the quick report from China Earthquake Network Center (CENC), the magnitude of the explosion was approximately M_L 2.2 and the focal depth was 0 km, occurred at 14:48:44 local time or 06:48:44 universal time (UTC), and with an epicentre 34.334°N 119.776°E . The explosion was caused by the chemical material stored in tanks located in a waste warehouse in Xiangshui chemical industry park, leading to massive casualties and property losses (*China Daily*; see the Data Availability section).

The seismology investigations on an explosive accident usually include the following: (i) determine its epicentre (e.g. Zhang & Wen 2013; Li & Tian 2015; Zhao *et al.* 2016; He *et al.* 2018); (ii) discriminate whether it is an explosion or an earthquake based on waveform characteristics (e.g. Kim & Richards 2007; Shin *et al.* 2010; Zhao *et al.* 2016, 2017; Walter *et al.* 2018; Ma *et al.* 2021); and (iii) calculate its magnitude and estimate its yield (e.g. Murphy *et al.* 2013; Zhang & Wen 2013; Zhao *et al.* 2016; Pasyanos & Myers 2018; Jiang *et al.* 2020). However, for the XEx, the estimated yields from different authors and organizations are rather scattered. For example, the State Key Laboratory of Explosion Science and Technology at the Beijing Institute of Technology and the No. 217

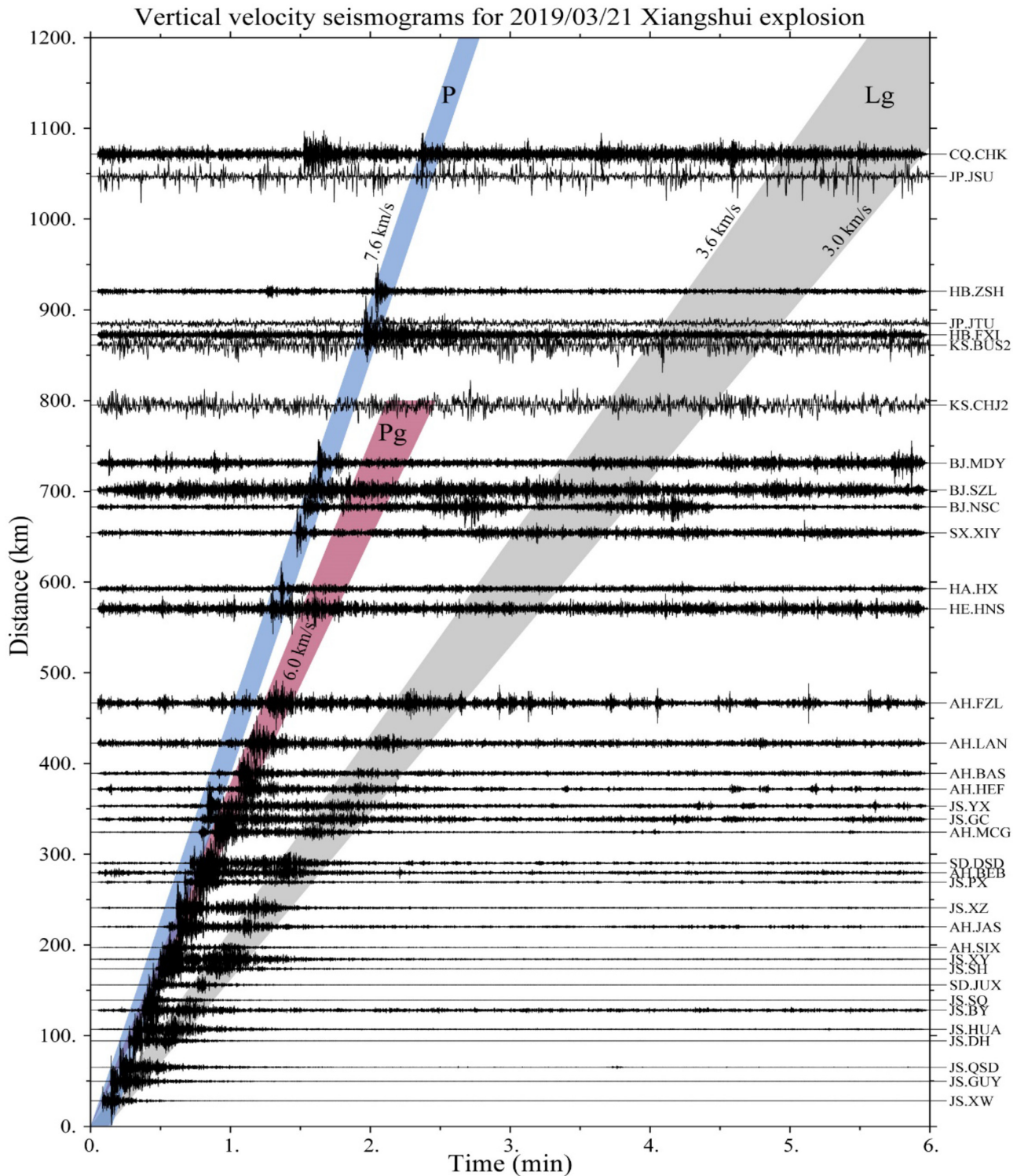


Figure 2. Normalized vertical-component velocity seismograms bandpass filtered between 5.0 and 10.0 Hz for the 2019 March 21 XEx. The traces are ordered according to their epicentral distances, with station names listed on the right side. The three shaded strips indicate *P*, *Pg* and *Lg* group velocity windows, respectively.

explosion were tested to estimate the explosive yield of XEx, and their results were compared. We also examined the applicability of the $m_b:M_s$ method and the *P/S* spectral ratio method for event discrimination in East China. The above results are also compared with those obtained in Northeast and Northwest China.

2 REGIONAL DATA SETS

The Xiangshui CEx generated abundant broad-band regional digital seismograms over distances from a few hundred to a few thousand kilometres (Fig. 2). Strong *P*-wave energy and relatively weak *Lg*

Table 1. Event parameters used in this study.

Event types	Date (yyyy/mm/dd)	Origin time (UTC) (hh:mm:ss)	Latitude (°N)	Longitude (°E)	Depth (km)	Catalogue magnitude or known yield (ton)	Rock type	Magnitude measurements					
								m_b (Lg)	SD	M_s	N		
Xiangshui explosion	2014/10/21	06:48:44	34.334	119.776	0.0	m_b 2.2	buried	3.39	0.24	1.95	55	0.27	37
Chemical explosion	2011/01/26	17:10:15	32.890	120.857	0.042	3.0 (ton)	Silt	2.63	0.33	2.24	43	0.18	51
	2011/01/22	19:00:14	34.641	118.651	0.071	3.5 (ton)	Silt	1.94	0.15	2.00	6	0.21	13
Nearby earthquake	2011/01/01	09:07:41	33.570	119.840	18.0	m_L 3.6	—	3.63	0.26	2.10	61	0.52	58
	2012/10/02	05:26:21	33.730	120.870	22.0	m_b 3.9	—	4.27	0.50	2.25	64	0.25	60
	2013/01/19	14:56:54	34.436	119.813	10.0	m_b 3.7	—	4.30	0.37	2.24	58	0.29	59
	2016/10/19	20:51:12	33.590	120.327	10.0	m_b 4.7	—	4.97	0.24	2.79	55	0.21	50

Note: N is number of records for calculating magnitudes and SD is their standard deviation.

phases can be seen from these waveforms, especially at remote stations, typical for shallow explosive sources (e.g. Richards & Kim 2007). In addition, on 2011 January 22 and 26, two nearby CExs were detonated in Dongtai Forest Farm, Yancheng City and Wenquan Town, Donghai County, Lianyungang City, both in Jiangsu Province, their yields being 3.5 and 3.0 ton in weight of ammonium nitrate explosive, respectively. The distances from the four NEqs to the XEx are 11.8, 85.2, 97.1 and 121.1 km. All NEqs occurred within the crust with local magnitudes between 3.9 and 4.7 reported by CENC. From all these events, we selected 703 broadband vertical-component seismograms recorded by 140 broad-band digital stations from several regional networks, including CNDNS, GSN, FDSN and F-net to investigate the characteristics of these explosions and earthquakes, including the yield estimation and event discrimination. All the event parameters are listed in Table 1, in which the parameters of the two nearby CExs are known.

Fig. 3 compares normalized vertical-component velocity seismograms from the XEx and two nearby CExs. These waveforms are recorded by stations at distances between 10 and 600 km and band-pass filtered between 5.0 and 10.0 Hz. They are characterized by abrupt P -wave arrivals and relatively weak Lg phases. In contrast, Fig. 4 shows records for four nearby earthquakes, whose waveforms are enriched in S -wave energy. Furthermore, Fig. 5 illustrates the velocity seismograms recorded at station XZ (Network JS), generated by the XEx, two nearby CExs and four nearby NEqs. For explosion sources, due to their isotropic mechanism, prominent P -wave onsets can be observed, whereas the S -type regional phases, such as the Sn and Lg, are nearly invisible. On the other hand, seismograms from nearby earthquakes are characterized by relatively weak P waves and strong Lg waves due to their shear dislocation mechanism. Different excitations of P and S waves from explosion and earthquake sources form the basis of the event discrimination.

3 MAGNITUDE MEASUREMENTS

We calculated both m_b (Lg) and M_s from Lg and regional Rayleigh waves. Following Zhao *et al.* (2008, 2012), the third peak (TP) amplitude method (Nuttli 1973, 1986) and rms amplitude method (Patton & Schlittenhardt 2005) were both applied to calculate the m_b (Lg) with

$$m_b(\text{Lg}) = 5.0 + \log [A(\Delta_0)/C], \quad (1)$$

where $A(\Delta_0)$ is the Lg wave amplitudes at a reference distance $\Delta_0 = 10$ km for an unknown magnitude event, and constant C is the amplitude for an $m_b = 5.0$ event at the reference distance. The values of C are 110 and 90 μm for the TP and rms methods, respectively (Nuttli 1973, 1986; Patton & Schlittenhardt 2005). To extrapolate the observed Lg wave amplitude $A(\Delta)$ to a reference distance Δ_0 , we use

$$A(\Delta_0) = A(\Delta) \cdot G(\Delta, \Delta_0) \cdot \Gamma(\Delta, \Delta_0, f), \quad (2)$$

where $G(\Delta, \Delta_0)$ is the geometrical spreading from Δ to Δ_0 , $\Gamma(\Delta, \Delta_0, f)$ is the attenuation factor along the great circle path from Δ_0 to Δ , and f is the frequency. For the TP method (Nuttli 1973, 1986)

$$G(\Delta, \Delta_0, \text{TP}) = (\Delta/\Delta_0)^{1/3} \times [\sin(\Delta/111.1)/\sin(\Delta_0/111.1)]^{1/2}, \quad (3)$$

and for the rms method (Yang 2002; Patton & Schlittenhardt 2005),

$$G(\Delta, \Delta_0, \text{rms}) = (\Delta/\Delta_0)^{1.0}. \quad (4)$$

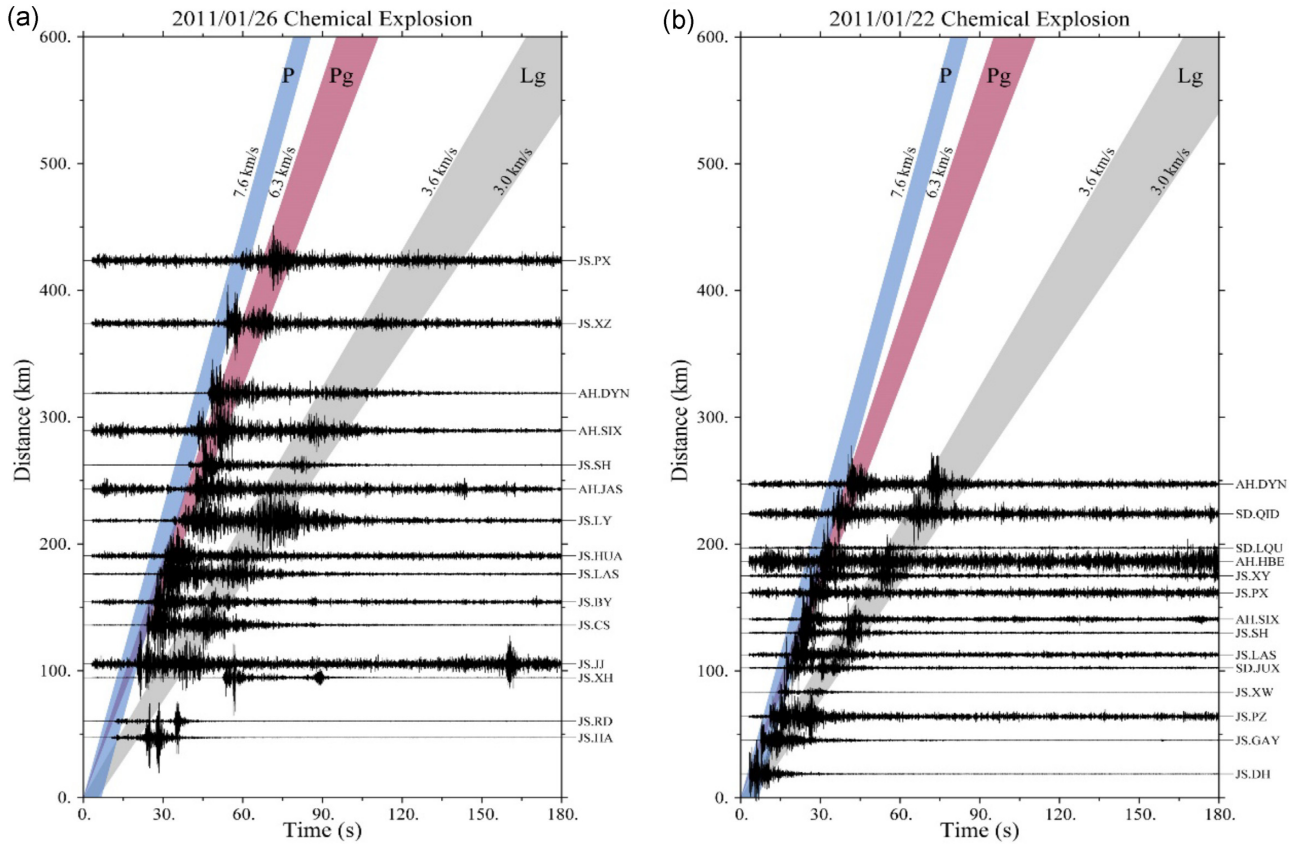


Figure 3. Comparisons of normalized vertical-component velocity seismograms bandpassed between 5.0 and 10.0 Hz for two nearby CExs occurred on 2011 January 26 (a) and 22 (b). The horizontal and vertical coordinates are time and epicentre distance. The P , Pg and Lg group velocities are indicated by shaded strips. Note that the waveforms show common features of clear impulsive P -wave onset and relatively weak Lg phases.

In eq. (2), the attenuation factor can be obtained by

$$\Gamma(\Delta, \Delta_0, f) = \exp\left[-\frac{\pi f}{V} \cdot \int_{\Delta_0}^{\Delta} \frac{ds}{Q(x, y, f)}\right], \quad (5)$$

where V is the Lg wave group velocity, $\int_{\Delta_0}^{\Delta} ds$ is the integral along the great circle path from Δ_0 to Δ , and $Q(x, y, f)$ is the quality factor of crustal media, a function of the frequency and surface location (x, y) . To calculate Γ , we adopted a high-resolution broadband Lg wave attenuation model for East China and its surrounding areas, as shown in Fig. 6 (Zhao *et al.* 2013).

Both Nuttli (1973, 1986) and Patton & Schlittenhardt (2005) measured the Lg wave amplitudes from vertical-component seismograms recorded by the World-Wide Standardized Seismograph Network short period instrument (WWSSN SP). To make our result consistent with previous studies, we first deconvolve the broadband instrument response from the digital seismic records and followed by convolve the seismograms with the WWSSN SP instrument response. Then, we picked Lg waves using a group velocity window between 3.6 and 3.0 km s⁻¹, from which both TP and rms amplitudes were measured. For the rms amplitude, the pre- P noise was also corrected (see, e.g. Zhao *et al.* 2008). Next, the observed amplitudes were extrapolated to the reference distance using eqs (2)–(5). A velocity of 3.5 km s⁻¹ is used as the nominal Lg wave group velocity, and the dominant frequency is obtained by counting the zero crossings. Finally, eq. (1) is used to calculate the Lg wave magnitude from both TP and the rms amplitudes. After correcting

station terms (Zhao *et al.* 2008), the magnitudes from individual stations were obtained and further averaged in the entire network to give the m_b (Lg , TP) and m_b (Lg , rms) for all events. The results are listed in Table 1.

Russell (2006) proposed a time-domain surface wave magnitude calculation method, which extended the usable frequency range to shorter periods and can be effectively used at both regional and teleseismic distances for magnitude-defining observations, which have been verified by many studies (Bonner *et al.* 2006, 2008; Chun *et al.* 2011; Fan *et al.* 2013). With this method, the vertical-component Rayleigh wave is first filtered by narrow band zero-phase Butterworth filter to generate multi-band signals with their central periods are between 8 and 25 s. From the maximum amplitude in each band, the magnitude M_s can be calculated using

$$M_s = \log A + \frac{1}{2} \log(\sin \Delta) + 0.0031 \left(\frac{20}{T}\right)^{1.8} \Delta - 0.66 \log\left(\frac{20}{T}\right) - \log f_c - 0.43, \quad (6)$$

where A is the maximum amplitude in nanometre after zero-phase Butterworth filtering. The Δ and T are the epicentral distance and period, $f_c \leq 0.6/T\sqrt{\Delta}$ is the corner frequency of the filter, and the corresponding passband of the filter is between $1/T - f_c$ and

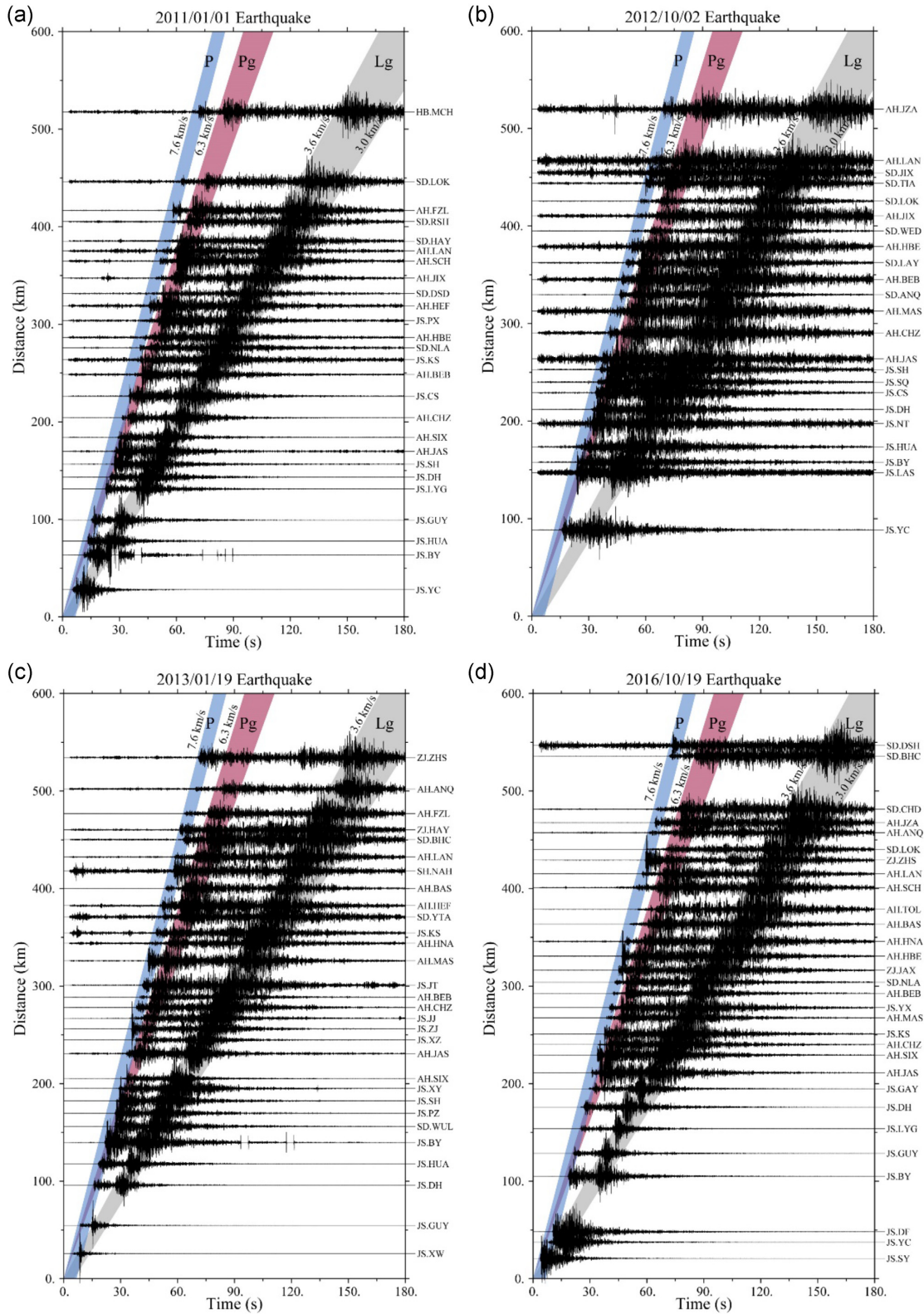


Figure 4. Similar to Fig. 3 except for four nearby earthquakes occurred on 2011 January 1 (a), 2011 October 2 (b), 2013 January 19 (c) and 2016 October 19 (d) recorded by stations listed on the right side. The waveforms are characterized by well-developed Lg phases.

$1/T + f_c$. The maximum magnitude from all passbands is chosen as the event magnitude at that station. In our case, we sample the Rayleigh waves using a group velocity window between 5.5 and 1.8 km s⁻¹. After removed the instrument response and

generated multiband surface waveforms, we calculated the site response to correct the waveform at each period, followed by using the above-mentioned method to calculate the station–event magnitude (Fan *et al.* 2013). Finally, the network averaged magnitude was

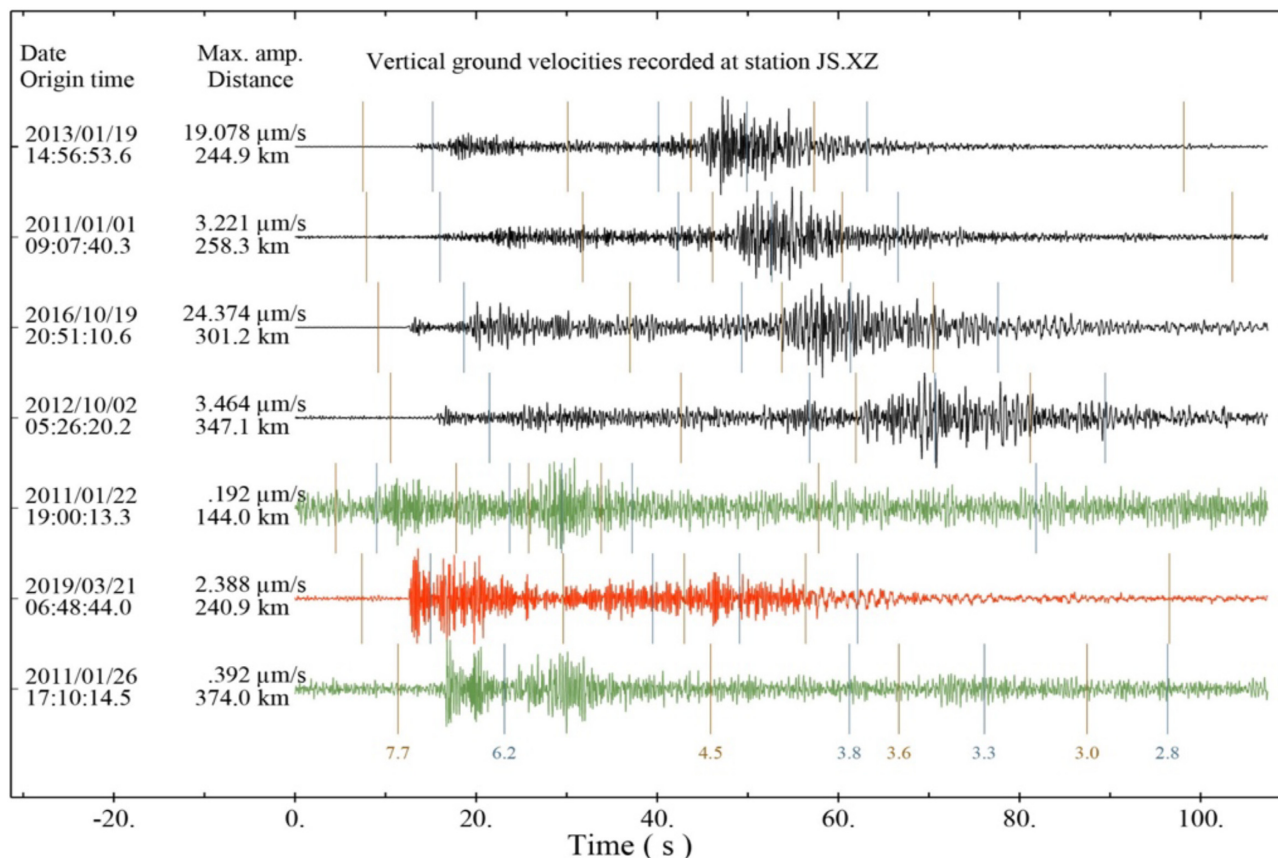


Figure 5. Normalized vertical-component velocity seismograms bandpassed between 5.0 and 10.0 Hz recorded at station XZ. Waveforms for four nearby earthquakes are shown in black, waveforms for two CEXs are shown in green and waveforms for the XEx are shown in red. The event dates, maximum amplitudes and epicentre distances are listed on the left. The vertical lines on the waveforms indicate the apparent group velocities. The seismograms from explosions show clear impulsive *P*-wave onsets, but *Sn* and *Lg* phases are nearly invisible. On the contrast, seismograms for the nearby earthquakes are characterized by relatively weak *P* waves and relatively strong *Lg* waves due to their shear dislocation source mechanisms.

obtained for each event. Rayleigh wave magnitudes obtained for all explosions and earthquakes are also listed in Table 1.

4 YIELD ESTIMATION

The yield estimation generally depends on the empirical relations between the yield and body wave magnitude from calibrated test sites, such as the m_b -yield relations for the Nevada test site (Nuttli 1986), Novaya Zemlya (Bowers *et al.* 2001), and East Kazakhstan (Ringdal *et al.* 1992; Murphy 1996). Based on the m_b (*Lg*) measurements, we adopted the above-mentioned three empirical magnitude-yield relations to estimate the seismic yield of the XEx. Fig. 7(a) shows these m_b (*Lg*)-yield relations and two nearby CEXs with known yields, which can provide reliable references at the low-yield end when choosing an empirical magnitude-yield relation for the XEx. For the CEXs, the reported yield is the weight of the ammonium nitrate explosive. From the figure, we can see that for explosions with body wave magnitudes between m_b 4 and 6, the magnitude-yield relations by different authors are very close. However, due to lack of small explosions, these empirical formulas differ by one to two orders of magnitudes at low-magnitude end. Considering that m_b (*Lg*) magnitude of XEx was small and the constraint of known-yield small CEXs at the low-yield end, we chose the empirical formulas by Bowers *et al.* (2001), Ringdal *et al.* (1992)

and Murphy (1996) to estimate the yield of the XEx and obtained a likely range between 37 and 133 ton (Fig. 7a).

However, considering that the storage tanks holding explosive chemicals is located above the ground, and the coupling between the source and the earth is not as tight as an underground explosion. Therefore, we turned to the fitting curve proposed by Ambrosini *et al.* (2002) for open-pit explosions, that is

$$\log\left(\frac{D/2}{|d|}\right) = 1.241 \log\left(\frac{Y^{1/3}}{|d|}\right) - 0.818, \quad (7)$$

where D and d are the diameter of the crater and the height of the burst in meters, respectively. According to the investigation report of accident investigation group of the State Council (see the Data Availability section), the diameter of the crater generated by the XEx is $D = 120$ m. The height of the burst should be the height of the centroid of explosive mass and is assumed to be 0.1–1 m. Y is the yield in kilogram. Fig. 7(b) illustrates the estimated yield for XEx based on eq. (7) with a possible range between 492 and 1884 ton. This result is close to the estimation of approximately 260 ton by the Beijing Institute of Technology and the No. 217 Research Institute at China North Industries Group Corporation. According to the accident investigation report, the XEx was caused by 600-ton nitration waste (see the Data Availability section). Thus, assuming that the explosive energy of the nitration waste equals to 0.3–0.5 TNT equivalent, the above estimations are roughly consistent with the ground truth information.

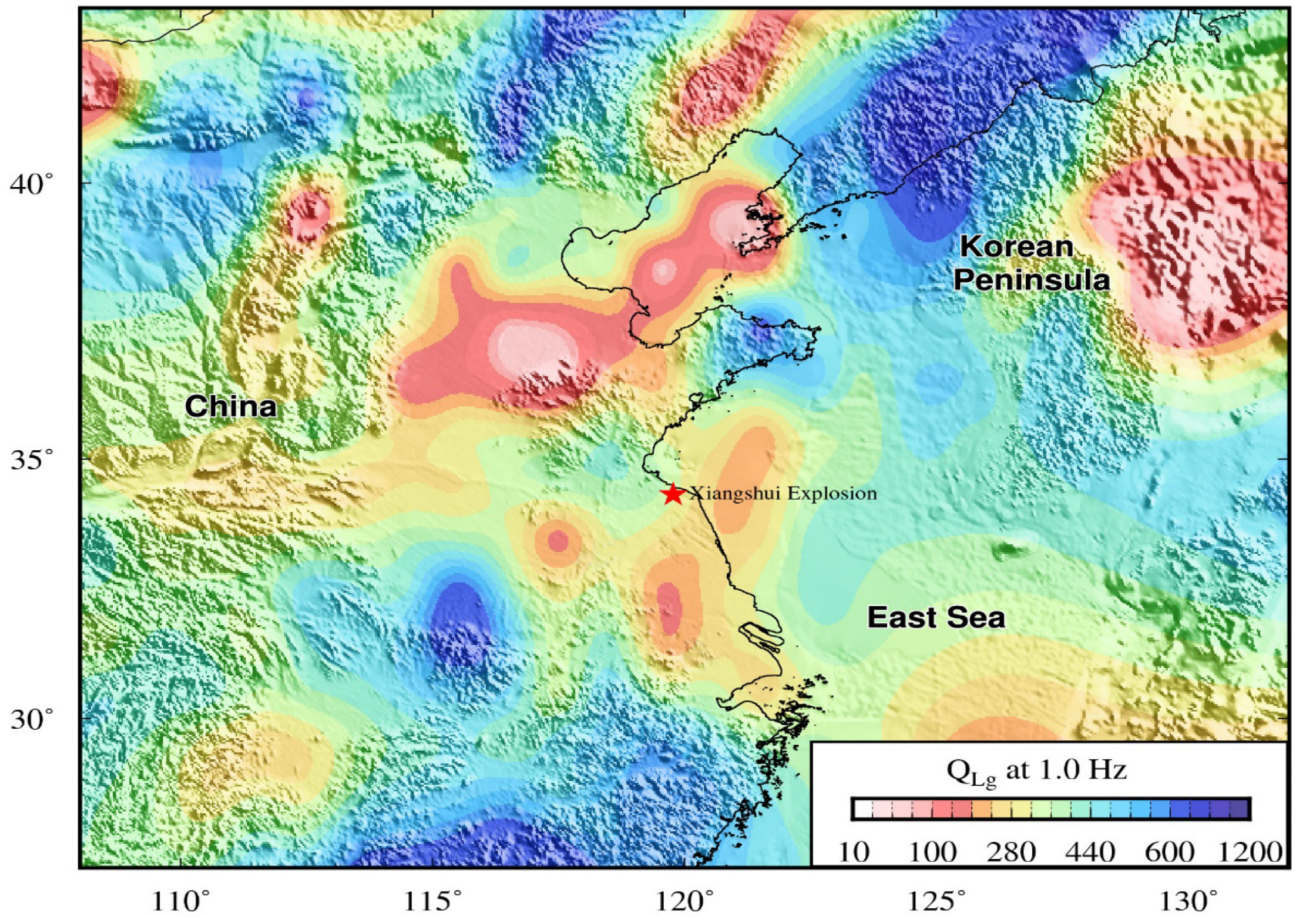


Figure 6. Crustal Lg wave Q map at 1.0 Hz for the investigated region (Zhao *et al.* 2013).

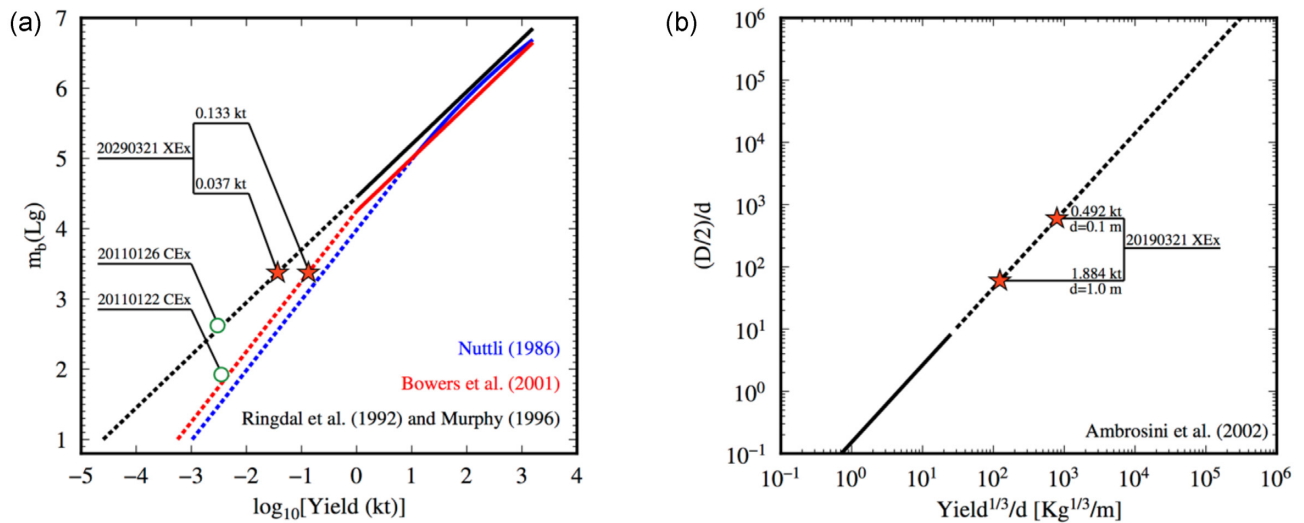


Figure 7. Empirical relations for yield estimation. Sections supported by observations are illustrated as solid lines, and extrapolations are illustrated as dashed lines. (a) Empirical magnitude–yield relations: the black line is from Ringdal *et al.* (1992) and Murphy (1996), the red line is from Bowers *et al.* (2001) and the blue line is from Nuttli (1986); XEx (red stars) estimated by black and red empirical relations and two CExs with known yields (green circles) are illustrated. (b) Fitting curve between the mass of the explosive yield, the diameter of the crater D and the height of the burst d from Ambrosini *et al.* (2002). The yield estimate results of XEx (red stars) assuming a burst height of 0.1 or 1.0 m.

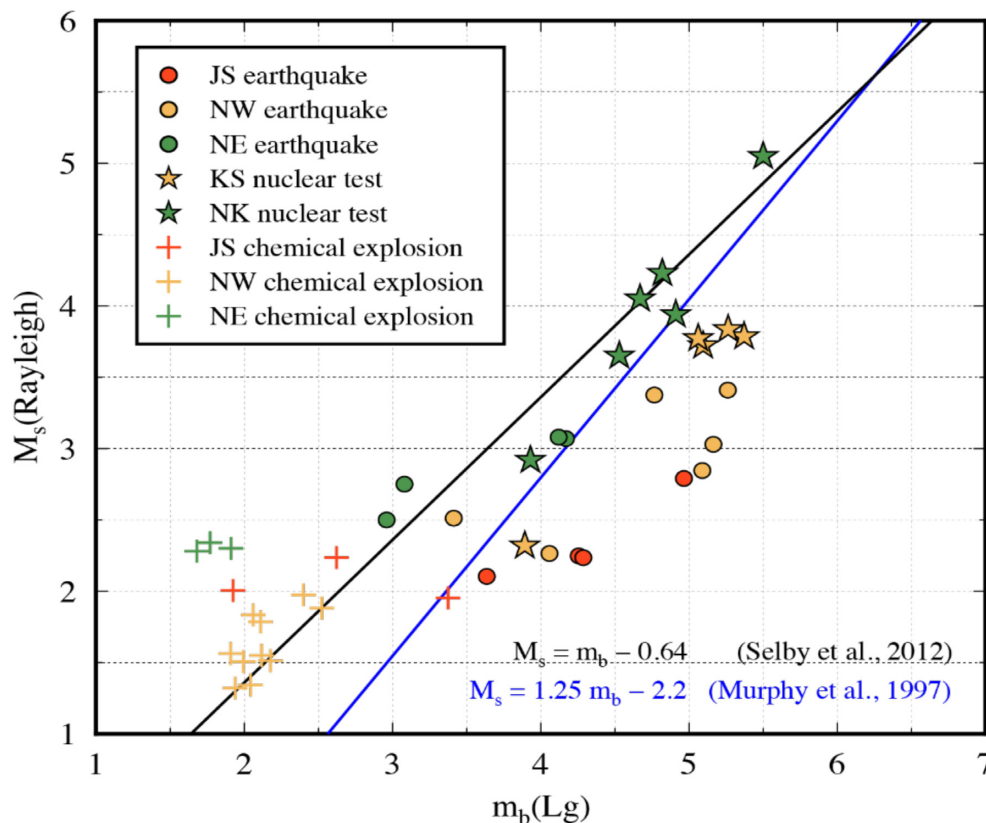


Figure 8. M_s versus m_b (Lg) for nuclear tests (solid stars), nearby NEqs (solid circles) and CExs (crosses) from Jiangsu Province, East China (red symbols), Northwest China and Semipalatinsk nuclear test site (yellow symbols), Northeast China and North Korea nuclear test site (green symbols). The m_b (Lg) and M_s of different regions are obtained from this study, Ma *et al.* (2021) and Xie & Zhao (2018). The black and blue lines are the screening criteria proposed by Murphy *et al.* (1997) and Selby *et al.* (2012) to distinguish explosions from earthquakes.

5 EVENT DISCRIMINATION

Discriminating explosions from NEqs relies on the difference in properties of these sources. An isotropic explosion source primarily generates P waves. In contrast, a shear dislocation earthquake source tends to generate strong S waves but weak P waves. These radiation features provide the physical basis for determining the property of seismic sources. Traditionally, the explosion source discrimination relies on the direct comparison between the teleseismic surface wave magnitude M_s and body wave magnitude m_b . This method has been demonstrated very effective for distinguishing large events at teleseismic distance (Stevens & Day 1985; Fisk *et al.* 2002; Bonner *et al.* 2011; Selby *et al.* 2012). However, at regional distances, due to the highly complicated excitation and propagation environment, the difference between body and surface wave magnitudes is no longer an effective index for discrimination (Bonner *et al.* 2008; Chun *et al.* 2011; Murphy *et al.* 2013; Zhao *et al.* 2017; Ma *et al.* 2021). Fig. 8 illustrates the M_s versus m_b (Lg) relation in different regions, including East China (this study), Northwest China with Semipalatinsk nuclear test site and Northeast China with North Korea nuclear test site (Xie & Zhao 2018; Ma *et al.* 2021). Apparently, the m_b (Lg)– M_s relation based on regional observations is not an effective discriminant in these regions.

On the other hand, the P/S spectral ratio method, including the Pg/Lg , Pn/Lg and Pn/Sn ratios, can largely eliminate the propagation effect and highlight the difference between different types of sources, and has been widely used for discrimination at regional distances (e.g. Taylor *et al.* 1989; Kim *et al.* 1993; Walter *et al.*

1995, 2007; Xie 2002; Fisk 2006; Richards & Kim 2007). Due to the fluctuations caused by certain local effects, observations from individual stations are often rather scattered and causing difficulties when used in the discrimination practice, especially for events deviated from the network centre, or for small events with very low signal-to-noise ratios (e.g. Richards & Kim 2007). Taking the advantage of densely distributed digital seismic networks in Northeast China, Zhao *et al.* (2016) conducted epicentral distance corrections to spectral ratios from individual stations. The results were normalized to a reference distance of 500 km and then their network averages were calculated. Compared to the single-station measurement, the epicentral distance corrected network average can largely eliminate the scatter of the results, effectively expand the available frequency band and greatly improve the reliability of discrimination (Zhao *et al.* 2016, 2017; He *et al.* 2018).

With the above method, we collected Pn , Pg , Sn and Lg waveforms from vertical-component regional seismograms at stations with purely continental paths. After eliminating the data with signal-to-noise ratios below 2.0, we calculated the network-averaged Pg/Lg , Pn/Lg and Pn/Sn spectral ratios for the XEx and two nearby CExs and four NEqs in East China. The results are analysed in Fig. 9, where Figs 9(a)–(c) compared spectral ratios from a CEx detonated on 2011 January 26 and an NEq that occurred on 2016 October 19. The network-averaged values and standard deviations were obtained from observed ratios at individual stations. Obviously, the network-averaged values are more stable than the single-station measurements. Next, we averaged the observed spectral ratios for all CExs and NEqs to create two reference curves, one

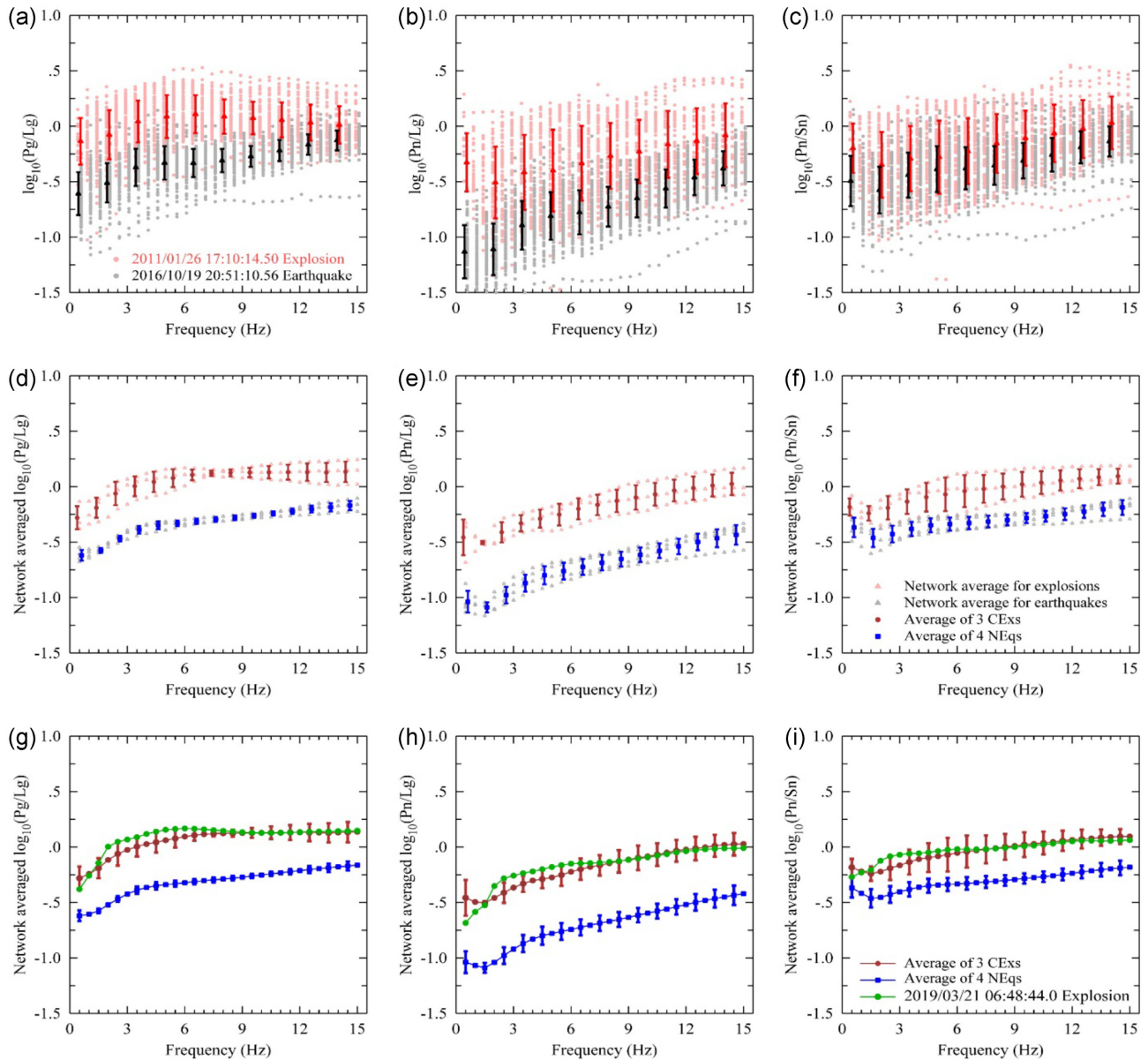


Figure 9. Spectral ratios for selected regional phases. (a–c) Comparisons of the Pg/Lg, Pn/Lg and Pn/Sn spectral ratios for a CEx detonated on 2011 January 26 (red) and a nearby NEq (black). Light coloured symbols are measurements from individual stations. Solid symbols and error bars show network-averaged values and their standard deviations, respectively. (d–f) Light red symbols are network-averaged ratios for individual CEXs, and light grey symbols are network-averaged ratios for individual NEqs. Solid symbols and error bars are mean values and standard deviations for the group of three CEXs (brown) and the group of four NEqs (blue). (g–i) Discrimination of the XEX (green) using the mean values from the CEX group (brown) and NEq group (blue).

for explosions and one for earthquakes, for event discrimination (Figs 9d–f). The reference curves illustrate apparent difference between the two source types. For all three types of spectral ratios, the explosion and earthquake populations can be fully separated by network-measured spectral ratios at frequencies above 2.0 Hz. As a discrimination test, Figs 9(g)–(i) illustrate the spectral ratios of XEX. They are very close to the reference curves of explosions, confirming it is an explosion. The above results suggested that, in East China, the P/S spectral ratio calculated at regional distances is a more reliable discriminant compared to the $m_b(Lg)-M_s$ method. It is worth noting that the XEX is an open-pit explosion, rather than nuclear tests that are mostly standard or overburied explosions.

Fig. 10 further compares the reference spectral ratios obtained in East China with those obtained in Northwest China (Ma *et al.* 2021) and Northeast China and the Korean Peninsula (He *et al.* 2018). Figs 10(a)–(c) show the reference Pg/Lg, Pn/Lg and Pn/Sn ratios from three small CEXs (brown) and four NEqs (blue) in East China. Figs 10(d)–(f) show similar results from 5 Semipalatinsk nuclear tests (red), 13 small CEXs (brown) and 6 NEqs (blue) in Northwest China and Semipalatinsk nuclear test site (Ma *et al.* 2021). In the bottom row, Figs 10(g)–(i) show the reference spectral ratios for six North Korean nuclear tests (red), three small CEXs (brown) and four NEqs in Northeast China and the Korean Peninsula (Zhao *et al.* 2008). In general, the nuclear explosion groups show the highest spectral ratios, whereas the NEqs display the lowest ratios. Small

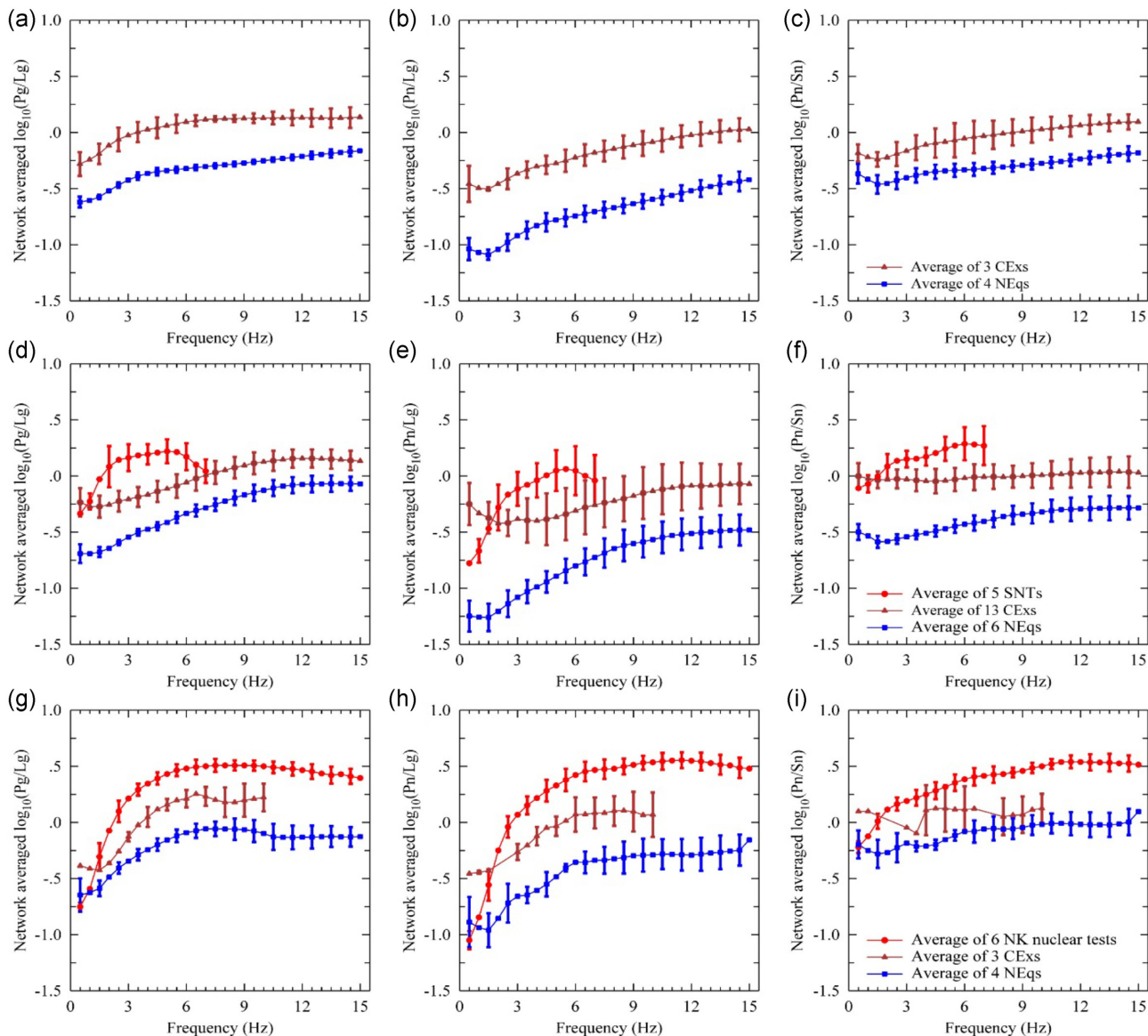


Figure 10. Comparisons of reference spectral ratios for Pg/Lg (left column), Pn/Lg (middle column) and Pn/Sn (right column) between different regions. (a–c) Solid symbols and error bars are average values and standard deviations from three CEExs (brown) and four NEQs (blue) in East China (refer to Figs 9d–f). (d–f) Similar results for 5 Semipalatinsk nuclear tests (red), 13 CEExs (brown) and 6 NEQs (blue) in Northwest China (Ma *et al.* 2021). (g–i) Similar results for six North Korean nuclear tests (red), three CEExs (brown) and four NEQs in Northeast China and the Korean Peninsula (blue) (He *et al.* 2018).

CEExs with a few to a few dozen tons of charge show spectral ratios higher than NEQs but usually lower than nuclear explosions. This phenomenon may be related to the P - and S -wave excitation mechanisms for explosion sources and depth dependence (e.g. Fisk 2006).

6 DISCUSSION AND CONCLUSION

Based on 703 vertical-component seismograms recorded at 140 broad-band digital seismic stations in East China and its surrounding regions, we investigated seismic characteristics of different source types, including XEx, two nearby small CEExs and four nearby NEQs. We used a regional data set and a broad-band Lg wave attenuation model (Zhao *et al.* 2013) to obtain the Lg wave and Rayleigh wave magnitudes for all events. The obtained body wave magnitude for

XEx is $m_b(\text{Lg}) = 3.39 \pm 0.24$, which is slightly higher than that given by previous studies (e.g. Jiang *et al.* 2020).

For the yield estimation of XEx, if the fully coupled hard-rock site equation by Bowers *et al.* (2001) is adopted, the yield from the Lg wave magnitude ranges between 37 and 133 ton. However, based on the crater size and an open-pit explosion equation (Ambrosini *et al.* 2002), the estimated yield is approximately 492 ton TNT equivalent, which is close to the 260 ton value by the Beijing Institute of Technology and the No. 217 Research Institute of the China North Industries Group Corporation. The apparently lower yield from seismic data compared to that from the ground truth results from the fact that the empirical magnitude–yield equation is for fully buried explosions, while the studied event is an open-pit explosion, which has a lower conversion rate in exciting seismic waves. Based on the above result, the explosion energy to seismic

energy conversion rate for the XEx is about one-third compared to that for a buried explosion.

Some previous studies suggested that the $m_b:M_s$ method does not provide effective discrimination in Northeast China, the Korean Peninsula and Northwest China when regional seismic data were used (e.g. Bonner *et al.* 2008; Zhao *et al.* 2017; Ma *et al.* 2021), while the P/S spectral ratios can successfully discriminate explosions from earthquakes (e.g. Taylor *et al.* 1989; Walter *et al.* 1995; Abdrakhmatov *et al.* 1996; Xie 2002; Fisk 2006; Richards & Kim 2007; Zhao *et al.* 2016; He *et al.* 2018; Pyle & Walter 2019; Ma *et al.* 2021). In this study, we calculated the network-averaged P/S discrimination at regional distance to check its capability in East China. Our results indicated that network-based spectral ratios work well at frequencies above 2.0 Hz to discriminate the explosions from the earthquake populations. However, for small event discrimination, both low-yield explosion and small-magnitude earthquake ($M < 3$) generate seismograms with high signal-to-noise ratio at local distance (< 150 km). Therefore, it is critical and challenging to explore discrimination techniques based on local observations (e.g. Koper *et al.* 2021).

ACKNOWLEDGEMENTS

The comments from editor M. Segou, assistant editor F. Storey and two reviewers are valuable and greatly improved this manuscript. This research was supported by the Special Fund of China Seismic Experimental Site (2019CSES0103 and 2016CESE0203) and the National Natural Science Foundation of China (41630210, 41674060, 41974054 and 41974061).

DATA AVAILABILITY

The waveforms recorded at CNDNS, GSN, FDSN and F-net stations used in this study were collected from CENC, the Data Management Center of China National Seismic Network at the Institute of Geophysics, China Earthquake Administration (SEISDMC, doi:10.7914/SN/CB; Zheng *et al.* 2010) at <http://www.seisdmc.ac.cn/> (last accessed August 2020), the Incorporated Research Institutions for Seismology Data Management Center (IRIS DMC) at www.iris.edu (last accessed August 2020) and the National Research Institute for Earth Science and Disaster Prevention (NIED) at <http://www.fnet.bosai.go.jp> (last accessed August 2020). The casualties and property losses can be referred to *China Daily*, available at <http://www.chinadaily.com.cn/a/201904/05/WS5ca7139ba3104842260b4983.html> (last accessed April 2019) and the Report on the 321 Explosion Accident in Xiangshui, Jiangsu Province, given by the accident investigation group of the State Council, available at <http://www.zjpy.gov.cn/art/2019/11/27/art.1440029.40543658.html> (last accessed July 2021). Some figures were made using Generic Mapping Tools (GMT; <https://forum.generic-mapping-tools.org/>, last accessed March 2021; Wessel *et al.* 2013).

REFERENCES

Abdrakhmatov, K.Y. *et al.*, 1996. Relatively recent construction of the Tien Shan inferred from GPS measurements of present-day crustal deformation rates, *Nature*, **384**, 450–453.
 Ambrosini, R.D., Luccioni, B.M., Danesi, R.F., Riera, J.D. & Rocha, M.M., 2002. Size of craters produced by explosive charges on or above the ground surface, *Shock Waves*, **12**, 69–78.

Bonner, J.L., Russell, D.R., Harkrider, D.G., Reiter, D.T. & Herrmann, R.B., 2006. Development of a time-domain, variable-period surface-wave magnitude measurement procedure for application at regional and teleseismic distances, part II: application and M_s-m_b performance, *Bull. seism. Soc. Am.*, **96**, 678–696.
 Bonner, J.L., Herrmann, R.B., Harkrider, D. & Pasyanos, M., 2008. The surface wave magnitude for the 9 October 2006 North Korean nuclear explosion, *Bull. seism. Soc. Am.*, **98**, 2498–2506.
 Bonner, J.L., Stroujkova, A. & Anderson, D., 2011. Determination of Love- and Rayleigh-wave magnitudes for earthquakes and explosions, *Bull. seism. Soc. Am.*, **101**, 3096–3104.
 Bowers, D., Marshall, P.D. & Douglas, A., 2001. The level of deterrence provided by data from the SPITS seismometer array to possible violations of the Comprehensive Test Ban in the Novaya Zemlya region, *Geophys. J. Int.*, **146**, 425–438.
 Chun, K.Y., Wu, Y. & Henderson, G.A., 2011. Magnitude estimation and source discrimination: a close look at the 2006 and 2009 North Korean underground nuclear explosions, *Bull. seism. Soc. Am.*, **101**, 1315–1329.
 Fan, N., Zhao, L.F., Xie, X.B. & Yao, Z.X., 2013. Measurement of Rayleigh-wave magnitudes for North Korean nuclear tests, *Chin. J. Geophys.*, **56**, 906–915.
 Fisk, M.D., 2006. Source spectral modeling of regional P/S discriminants at nuclear test sites in China and the former Soviet Union, *Bull. seism. Soc. Am.*, **96**, 2348–2367.
 Fisk, M.D., Jepsen, D. & Murphy, J.R., 2002. Experimental seismic event-screening criteria at the prototype International Data Center, *Pure appl. Geophys.*, **159**, 865–888.
 He, X., Zhao, L.F., Yao, Z.X. & Xie, X.B., 2018. High-precision relocation and event discrimination for the 3 September 2017 underground nuclear explosion and subsequent seismic events at the North Korean test site, *Seismol. Res. Lett.*, **89**, 2042–2048.
 Jiang, W.B., Chen, Y. & Peng, F., 2020. The yield estimation of the explosion at the Xiangshui, Jiangsu chemical plant in March 2019, *Chin. J. Geophys.*, **63**, 541–550 (in Chinese).
 Kim, W.Y. & Richards, P.G., 2007. North Korean nuclear test: seismic discrimination at low yield, *EOS, Trans. Am. geophys. Un.*, **88**, 158.
 Kim, W.Y., Simpson, D.W. & Richards, P.G., 1993. Discrimination of earthquakes and explosions in the eastern United States using regional high-frequency data, *Geophys. Res. Lett.*, **20**, 1507–1510.
 Koper, K.D., Holt, M.M., Voyles, J.R., Burlacu, R., Pyle, M.L., Wang, R.J. & Schmandt, B., 2021. Discrimination of small earthquakes and buried single-fired chemical explosions at local distances (< 150 km) in the Western United States from comparison of local magnitude (M_L) and coda duration magnitude (M_C), *Bull. seism. Soc. Am.*, **111**, 558–570.
 Li, J. & Tian, B.F., 2015. Refined locations of major explosions in Tianjin Harbor, *Sci. Bull.*, **60**, 1868–1870.
 Ma, X., Zhao, L.-F., Xie, X.-B., He, X. & Yao, Z.-X., 2021. Regional seismic characteristics of chemical explosions on the eastern margin of the Junggar Basin, Northwest China, and of historical Semipalatinsk nuclear tests, *Bull. seism. Soc. Am.*, **111**, 606–620.
 Murphy, J.R., 1996. Types of seismic events and their source descriptions, in *Monitoring a Comprehensive Test Ban Treaty*, pp. 225–245, eds Husebye, E.S. & Dainty, A.M., Kluwer Academic Publisher.
 Murphy, J.R., Barker, B.W. & Marshall, M.E., 1997. Event screening at the IDC using the M_s/m_b discriminant, Maxwell Technologies Final Report, 23pp.
 Murphy, J.R., Stevens, J.L., Kohl, B.C. & Bennett, T.J., 2013. Advanced seismic analyses of the source characteristics of the 2006 and 2009 North Korean nuclear tests, *Bull. seism. Soc. Am.*, **103**, 1640–1661.
 Nuttli, O.W., 1973. Seismic wave attenuation and magnitude relations for eastern North America, *J. geophys. Res.*, **78**, 876–885.
 Nuttli, O.W., 1986. Yield estimates of Nevada test site explosions obtained from seismic Lg waves, *J. geophys. Res.*, **91**, 2137–2151.
 Pasyanos, M.E. & Myers, S.C., 2018. The coupled location/depth/yield problem for North Korea's declared nuclear tests, *Seismol. Res. Lett.*, **89**, 2059–2067.

- Patton, H.J. & Schlittenhardt, J., 2005. A transportable $m_b(Lg)$ scale for central Europe and implications for low-magnitude M_s - m_b discrimination, *Geophys. J. Int.*, **163**, 126–140.
- Pyle, M. & Walter, W., 2019. Investigating the effectiveness of P/S amplitude ratios for local distance event discrimination, *Bull. seism. Soc. Am.*, **109**, doi:10.1785/0120180256.
- Richards, P.G. & Kim, W.Y., 2007. Seismic signature, *Nat. Phys.*, **3**, 4–6.
- Ringdal, F., Marshall, P.D. & Alewine, R.W., 1992. Seismic yield determination of Soviet underground nuclear explosions at the Shagan River test site, *Geophys. J. Int.*, **109**, 65–77.
- Russell, D.R., 2006. Development of a time-domain, variable-period surface-wave magnitude measurement procedure for application at regional and teleseismic distances, part I: theory, *Bull. seism. Soc. Am.*, **96**, 665–677.
- Selby, N.D., Marshall, P.D. & Bowers, D., 2012. $m_b:M_s$ event screening revisited, *Bull. seism. Soc. Am.*, **102**, 88–97.
- Shin, J.S., Sheen, D.-H. & Kim, G., 2010. Regional observations of the second North Korean nuclear test on 2009 May 25, *Geophys. J. Int.*, **180**, 243–250.
- Stevens, J.L. & Day, S.M., 1985. The physical basis of $m_b:m_s$ and variable frequency magnitude methods for earthquake/explosion discrimination, *J. geophys. Res.*, **90**, 3009.
- Taylor, S.R., Denny, M.D., Vergino, E.S. & Glaser, R.E., 1989. Regional discrimination between NTS explosions and western U.S. earthquakes, *Bull. seism. Soc. Am.*, **79**, 1142–1176.
- Walter, W.R., Mayeda, K.M. & Patton, H.J., 1995. Phase and spectral ratio discrimination between NTS earthquakes and explosions. Part 1: empirical observations, *Bull. seism. Soc. Am.*, **85**, 1050–1067.
- Walter, W.R., Matzel, E., Pasyanos, M.E., Harris, D.B., Gok, R. & Ford, S.R., 2007. Empirical observations of earthquake-explosion discrimination using P/S ratios and implications for the sources of explosion S -waves, in *Proceedings of the 29th Monitoring Research Review: Ground-Based Nuclear Explosion Monitoring Technologies*, Denver, CO, pp. 684–693.
- Walter, W.R., Dodge, D.A., Ichinose, G., Myers, S.C., Pasyanos, M.E. & Ford, S.R., 2018. Body-wave methods of distinguishing between explosions, collapses, and earthquakes: application to recent events in North Korea, *Seismol. Res. Lett.*, **89**, 2131–2138.
- Wessel, P., Smith, W.H.F., Scharroo, R., Luis, J. & Wobbe, F., 2013. Generic mapping tools: improved version released, *EOS, Trans. Am. geophys. Un.*, **94**, 409–410.
- Xie, J.K., 2002. Source scaling of Pn and Lg spectra and their ratios for explosions in central Asia: implications for the identification of small seismic events at regional distances, *J. geophys. Res.*, **107**, ESE 1–1, doi:10.1029/2001jb000509.
- Xie, X.B. & Zhao, L.F., 2018. The seismic characterization of North Korea underground nuclear tests, *Chin. J. Geophys.*, **61**, 889–904.
- Yang, X., 2002. A numerical investigation of Lg geometrical spreading, *Bull. seism. Soc. Am.*, **92**, 3067–3079.
- Zhang, M. & Wen, L.X., 2013. High-precision location and yield of North Korea's 2013 nuclear test, *Geophys. Res. Lett.*, **40**, 2941–2946.
- Zhao, L.F., Xie, X.B., Wang, W.M. & Yao, Z.X., 2008. Regional seismic characteristics of the 9 October 2006 North Korean nuclear test, *Bull. seism. Soc. Am.*, **98**, 2571–2589.
- Zhao, L.F., Xie, X.B., Wang, W.M. & Yao, Z.X., 2012. Yield estimation of the 25 May 2009 North Korean nuclear explosion, *Bull. seism. Soc. Am.*, **102**, 467–478.
- Zhao, L.F., Xie, X.B., Wang, W.M., Zhang, J.H. & Yao, Z.X., 2013. Crustal Lg-wave attenuation within the North China Craton and its surrounding regions, *Geophys. J. Int.*, **195**, 513–531.
- Zhao, L.F., Xie, X.B., Wang, W.M., Hao, J.L. & Yao, Z.X., 2016. Seismological investigation of the 2016 January 6 North Korean underground nuclear test, *Geophys. J. Int.*, **206**, 1487–1491.
- Zhao, L.F., Xie, X.B., Wang, W.M., Fan, N., Zhao, X. & Yao, Z.X., 2017. The 9 September 2016 North Korean underground nuclear test, *Bull. seism. Soc. Am.*, **107**, 3044–3051.
- Zheng, X., Jiao, W., Zhang, C. & Wang, L., 2010. Short-period Rayleigh-wave group velocity tomography through ambient noise cross-correlation in Xinjiang, Northwest China, *Bull. seism. Soc. Am.*, **100**, 1350–1355.